Traversing the Slopes of Phase Space with `ALPS`: Linear Dispersion Relations from Plasma Peaks to Gravitational Valleys

K.G. Klein[1]†,

[1]Lunar and Planetary Laboratory, University of Arizona, Tucson, AZ 85750, USA

`ALPS` (the Arbitrary Linear Plasma Solver) is a parallelised numerical code that solves the Vlasov-Maxwell dispersion relation for hot (even relativistic) magnetised plasmas. `ALPS` allows for any number of particle species or components with arbitrary gyrotropic equilibrium velocity distribution functions supporting waves with any direction of propagation with respect to the background magnetic field $\mathbf{B}$. In this set of notes prepared for the KITP 2024 "Interconnections between the Physics of Plasmas and Self-gravitating Systems" program, we introduce the underlying method, describe some of the numerical implementations, discuss open problems, and attempt to identify potential overlaps with adjacent fields. *Caveat lector*, as typographical error likely abound through this draft.

1. Introduction

Numerical plasma dispersion solvers have been extensively used to study plasma waves, in particular their growth or damping rates as a function of plasma conditions (see Gary 1993; Verscharen *et al.* 2013; Klein *et al.* 2017; Klein *et al.* 2021; McManus *et al.* 2024, for a biased selection of mostly space plasma studies). Typical linear plasma dispersion solvers assume a particular analytic form for the underlying velocity distribution (VDF) $f_j(\mathbf{v})$, e.g. a bi-Maxwellian (`WHAMP` (Roennmark 1982), `PLUME` (Klein & Howes 2015), or `NHDS` (Verscharen & Chandran 2018)) or a bi-Kappa (`DSHARK` (Astfalk *et al.* 2015)) distribution. Such an assumption enables a closed form expression in terms of known special functions for the integrals embedded within the dispersion relation. However, many space and astrophysical plasmas, or other hot and diffuse plasmas, are not well represented by bi-Maxwellian, or even bi-Kappa, distributions. Thus, a more sophisticated treatment of the dispersion relation is required.

The Arbitrary Linear Plasma Solver (`ALPS`), recently made publicly available and open source (BSD 2 license) (Klein *et al.* 2023) can determine complex-valued dispersion relations for plasma waves associated with arbitrary VDFs. The initial `ALPS` implementation is described in Verscharen *et al.* (2018), though some additions to the code has been made since publication, some of which are described in these notes (which will be be detailed in future publications).

`ALPS` is an MPI parallelised numerical code written in `FORTRAN90` that solves the Vlasov-Maxwell dispersion relation for a hot, magnetized plasma. `ALPS` allows for any number of particle species with arbitrary gyrotropic equilibrium distribution functions supporting waves with any direction of propagation with respect to the background magnetic field, and `ALPS` can include the effects of special relativity in the plasma response.

† Email address for correspondence: kgklein@arizona.edu

Instead of using parameterized values for a collection of analytic functions, `ALPS` uses as input the phase-space density on a discrete grid of parallel and perpendicular velocity $f_s(v_\perp, v_\parallel)$, (or momentum grid for relativistic calculations $f_s(p_\perp, p_\parallel)$), and evaluates the dispersion relation through a direct numerical integration of the gradients of f_s. This method has been applied to spacecraft data from both MMS (Jiang *et al.* 2022, 2024) and Wind (Walters *et al.* 2023), showing significant deviations of wave behavior from predictions calculated using simple analytic functions.

Aspects of this code address two of the workshop's focus topics:

- **Stability & Landau damping** – how can we compute the dispersion relation and stability of a general kinetic equilibrium?
- **Numerical methods and diagnostics** – how can we use numerical simulations to advance theoretical frameworks and to understand their potential pitfalls?

2. Underlying Equations

2.1. *Wave Equation*

As we are working with moving charged particles, we will need to invoke Maxwell's equations for the spatial and temporal variations of the electric and magnetic fields $\mathbf{E}$ and $\mathbf{B}$, specifically Ampere:

$$\nabla \times \mathbf{B} = \frac{4\pi \mathbf{j}}{c} + \frac{1}{c}\frac{\partial \mathbf{E}}{\partial t} = \frac{1}{c}\frac{\partial \mathbf{D}}{\partial t} \tag{2.1}$$

and Faraday

$$\nabla \times \mathbf{E} = -\frac{1}{c}\frac{\partial \mathbf{B}}{\partial t}. \tag{2.2}$$

Assuming we have a spatially homogeneous system, and have plane wave solutions of the form $\exp[i(\mathbf{k} \cdot \mathbf{r} - \omega t)]$, where $\omega = \omega_{\rm r} + i\gamma$ is the complex frequency and $\mathbf{k}$ is wavevector, the electric displacement $\mathbf{D}$ is related to the electric field via the dielectric tensor $\underline{\underline{\epsilon}}$

$$\mathbf{D}(\omega, \mathbf{k}) = \underline{\underline{\epsilon}}(\omega, \mathbf{k}) \cdot \mathbf{E}(\omega, \mathbf{k}). \tag{2.3}$$

The dielectric tensor is comprised by the summation over the contributions from the constituent plasma components:

$$\underline{\underline{\epsilon}}(\omega, \mathbf{k}) = \underline{\underline{1}} + \sum_s \underline{\underline{\chi}}_s(\omega, \mathbf{k}) \tag{2.4}$$

where $\underline{\underline{\chi}}_s$ is the susceptibility of the $s^{\rm th}$ plasma component, defined below.

We can perform the *usual* Fourier analysis, and combine Eqns. 2.1 and 2.2 to homogeneous plasma wave equation

$$\mathbf{k} \times (\mathbf{k} \times \mathbf{E}) + \frac{\omega^2}{c^2}\underline{\underline{\epsilon}} \cdot \mathbf{E} = 0. \tag{2.5}$$

or written more compactly as

$$\underline{\underline{\Lambda}} \cdot \mathbf{E} = \begin{pmatrix} \epsilon_{xx} - n_z^2 & \epsilon_{xy} & \epsilon_{xz} + n_x n_z \\ \epsilon_{yx} & \epsilon_{yy} - n_x^2 - n_z^2 & \epsilon_{yz} \\ \epsilon_{zx} + n_x n_z & \epsilon_{zy} & \epsilon_{zz} - n_x^2 \end{pmatrix} \begin{pmatrix} E_x \\ E_y \\ E_z \end{pmatrix} = 0. \tag{2.6}$$

where $\mathbf{n} = c\mathbf{k}/\omega$ is the index of refraction. The solutions of $\det |\Lambda(\omega, \mathbf{k})| = 0$ are the normal modes supported by the prescribed equilibrium.

The total plasma current $\mathbf{j}$ is defined in terms of the plasma component bulk velocities $\mathbf{U}_s$

$$\mathbf{j} = \sum_s \mathbf{j}_s = \sum_s n_s q_s \mathbf{U}_s \qquad (2.7)$$

where the density and electric charge of the components are n_s and q_s respectively.

By relating the current to the susceptibility via

$$\mathbf{j}_s = -\frac{i\omega}{4\pi} \underset{=s}{\chi} \cdot \mathbf{E}. \qquad (2.8)$$

we will be able to connect the wave equation to the distribution of the plasma particles, as discussed in the following subsection.

2.2. *The Hot, Magnetized, Plasma Dispersion Relation*

To quantify the impact of the shape of the velocity distribution $f_s(\mathbf{r}, \mathbf{p}, t)$† on the linear modes supported by a plasma equilibrium, we note that the bulk velocity utilized in Eqn. 2.7 is simply the first moment of the perturbed VDF δf ‡

$$\mathbf{j} = \sum_s \mathbf{j}_s = \sum_s q_s \int d^3\mathbf{p}\mathbf{v}\delta f_s(\mathbf{r}, \mathbf{p}, t) = -\frac{i\omega}{4\pi} \underset{=s}{\chi} \cdot \mathbf{E} \qquad (2.9)$$

where the VDF has been decomposed into a time averaged equilibrium and a first-order perturbation

$$f_s(\mathbf{r}, \mathbf{p}, t) = f_{0,s}(\mathbf{p}) + \delta f_s(\mathbf{r}, \mathbf{p}, t). \qquad (2.10)$$

The VDF for a collisionless plasma evolves according to the Vlasov equation

$$\frac{\partial f_s}{\partial t} + \mathbf{v} \cdot \frac{\partial f_s}{\partial \mathbf{r}} + q_s \left(\mathbf{E} + \frac{\mathbf{v}}{c} \times \mathbf{B} \right) \cdot \frac{\partial f_s}{\partial \mathbf{p}} = 0. \qquad (2.11)$$

For a particle trajectory $\mathbf{r}(t)$, the rate of change of f along the trajectory is

$$\frac{df}{dt} = \frac{\partial f}{\partial t} + \frac{\partial f}{\partial \mathbf{r}} \cdot \frac{d\mathbf{r}}{dt} + \frac{\partial f}{\partial \mathbf{p}} \cdot \frac{d\mathbf{p}}{dt}. \qquad (2.12)$$

In a static magnetic field, the zero-order trajectory of a charged particle is

$$\frac{d\mathbf{r}}{dt} = \mathbf{v} \text{ and } \frac{d\mathbf{p}}{dt} = q_s \frac{\mathbf{v}}{c} \times \mathbf{B}_0, \qquad (2.13)$$

which allows us to assert by inspection of the Vlasov equation that the equilibrium distribution is time stationary

$$\left(\frac{df_{s,0}}{dt} \right)_0 = 0. \qquad (2.14)$$

The first order Vlasov equation for the rate of change of the perturbed VDF along the zero-order trajectory is

$$\left(\frac{d\delta f_s}{dt} \right)_0 = -q_s \left(\mathbf{E}_1 + \frac{\mathbf{v}}{c} \times \mathbf{B}_1 \right) \cdot \frac{\partial f_{s,0}}{\partial \mathbf{p}}, \qquad (2.15)$$

which admits a solution for the perturbed distribution via integration along the trajectory

$$\delta f_s(\mathbf{r}, \mathbf{p}, t) = -q_s \int_{-\infty}^{t} dt' \left[\mathbf{E}_1(\mathbf{r}', t') + \frac{\mathbf{v}'}{c} \times \mathbf{B}_1(\mathbf{r}', t') \right] \cdot \frac{\partial f_{s,0}(\mathbf{p}')}{\partial \mathbf{p}'} \qquad (2.16)$$

† `ALPS` evaluates f_s on a momentum, rather than velocity grid to ease the transition to the relativistic limit.

‡ A detailed derivation is presented in Chapter 10 of Stix (1992).

Following *several* pages of identities, transformations, and substitutions, we arrive at an expression for the susceptibility in terms of integrals over functions of momentum derivatives of the equilibrium VDF

$$\underline{\underline{\chi}}_s = \frac{\omega_{p,s}^2}{\omega \Omega_{0,s}} \int_0^\infty 2\pi p_\perp dp_\perp \int_{-\infty}^\infty dp_\parallel \tag{2.17}$$

$$\left[\hat{e}_\parallel \hat{e}_\parallel \frac{\Omega_j]s}{\omega} \left(\frac{1}{p_\parallel} \frac{\partial f_{s,0}}{\partial p_\parallel} - \frac{1}{p_\perp} \frac{\partial f_{s,0}}{\partial p_\perp} \right) p_\parallel^2 + \sum_{n=-\infty}^\infty \frac{\Omega_s p_\perp U}{\omega - k_\parallel v_\parallel - n\Omega_s} \underline{\underline{T}}_n \right]$$

where we define the functions

$$U = \frac{\partial f_{0,s}}{\partial p_\perp} + \frac{k_\parallel}{\omega} \left(v_\perp \frac{\partial f_{0,s}}{\partial p_\parallel} - v_\parallel \frac{\partial f_{0,s}}{\partial p_\perp} \right) \tag{2.18}$$

and

$$\underline{\underline{T}}_n = \begin{pmatrix} \frac{n^2 J_n^2}{z^2} & \frac{i n J_n J_n'}{z} & \frac{n J_n^2 p_\parallel}{z p_\perp} \\ -\frac{i n J_n J_n'}{z} & (J_n')^2 & \frac{-i J_n J_n' p_\parallel}{p_\perp} \\ \frac{n J_n^2 p_\parallel}{z p_\perp} & \frac{i J_n J_n' p_\parallel}{p_\perp} & \frac{J_n^2 p_\parallel^2}{p_\perp^2} \end{pmatrix}. \tag{2.19}$$

The directions $\parallel$ and $\perp$ are defined with respect to the mean magnetic field direction $\mathbf{B}_0$. J_n is the nth order Bessel function with argument $z = k_\perp v_\perp / \Omega_s$. Two characteristic timescales are defined in terms of the plasma frequency $\omega_{ps} = \sqrt{4\pi n_s q_s^2 / m_j}$ and the cyclotron frequency $\Omega_s = q_s B_0 / m_s c$; $\Omega_{0,s}$ only includes the rest-mass in the denominator, while Ω_s includes the appropriate relativistic correction. Most traditional approaches further reduce Eqn. 2.17 by assuming an analytic form for $f_{0,s}$ that simplifies the integrals. ALPS instead directly integrates these derivatives encoded in this equation on a user defined discrete grid. There are two particular issues that arise in this numerical evaluation for the non-relativistic† case that must be handled carefully, dealing with the integration near poles (§3.1) and the handling of the analytic continuation of the integral into the complex plane (§3.2).

3. Numerical Implementation

After reading the velocity distribution values in on a user defined grid in $(p_\perp, p_\parallel)$, ALPS will either accept user inputs for N initial guesses for the complex frequencies $\omega = (\omega_{\rm r}, \gamma)$ that satisfy the wave equation or will solve Eqn 2.5 over a specified grid of $(\omega_{\rm r}, \gamma)$ values, and then identify the first N solutions that satisfy $\det |\Lambda(\omega, \mathbf{k})| = 0$. With these N solutions identified, ALPS will perform 1D wavevector scans,

- for fixed $k_\perp$ and varying $k_\parallel$, fixed $k_\parallel$ and varying $k_\perp$,
- for fixed $\theta = \arctan k_\perp / k_\parallel$ and varying $|k|$,
- between two specified $(k_\perp, k_\parallel)$ values,

or a 2D wavevector scan over specified ranges of $k_\perp$ and $k_\parallel$.

With the complex frequency determined, the complete eigenfunction of the densities δn_s, velocities $\delta \mathbf{U}_s$, and electromagnetic fields $\mathbf{E}$ and $\mathbf{B}$ can be calculated through evaluations of the linearized Maxwell's equations, the continuity equation, and the wave equation Eqn. 2.5, using the routines implemented in PLUME(Klein & Howes 2015).

We choose the complex Fourier coefficient for $\hat{E}_x \equiv E_x / E_{\perp,1} = 1$, where $E_{\perp,1}$ is an arbitrary real constant used to specify the overall amplitude of the linear eigenfunction,

† For the relativistic issues, see §3.3 of Verscharen *et al.* (2018).

and solve for the other components using Eqn. (2.5) in terms of $E_{\perp,1}$, yielding

$$\hat{E}_{||} \equiv \frac{E_{||}}{E_{\perp,1}} = \frac{\Lambda_{yx}\Lambda_{zy} - \Lambda_{yy}\Lambda_{zx}}{\Lambda_{yy}\Lambda_{zz} - \Lambda_{yz}\Lambda_{zy}} \tag{3.1}$$

and

$$\hat{E}_{\perp,2} \equiv \frac{E_{\perp,2}}{E_{\perp,1}} = -\frac{\Lambda_{zx} + \Lambda_{zz}(E_{||}/E_{\perp,1})}{\Lambda_{zy}} = \frac{\Lambda_{zx}\Lambda_{yz} - \Lambda_{zz}\Lambda_{yx}}{\Lambda_{yy}\Lambda_{zz} - \Lambda_{yz}\Lambda_{zy}}, \tag{3.2}$$

where Λ_{ij} are the elements of the 3×3 matrix $\underline{\underline{\Lambda}}$ dispersion tensor in (2.6).

Combining these solutions for the complex Fourier coefficients of the components of $\mathbf{E}$ with the solutions for the complex frequency ω and wave vector $\mathbf{k} = k_\perp \hat{\mathbf{x}} + k_{||}\hat{\mathbf{z}}$, we can solve for the complex Fourier coefficients of the magnetic field eigenfunction using the Faraday's Law, Eqn. 2.2, Fourier transformed in time and space, $\omega\mathbf{B} = c\mathbf{k} \times \mathbf{E}$, giving

$$\frac{B_{\perp,1}}{E_{\perp,1}} = -\frac{ck_{||}(E_{\perp,2}/E_{\perp,1})}{\omega}, \tag{3.3}$$

$$\frac{B_{\perp,2}}{E_{\perp,1}} = \frac{ck_{||} - ck_\perp(E_{||}/E_{\perp,1})}{\omega}, \tag{3.4}$$

and

$$\frac{B_{||}}{E_{\perp,1}} = \frac{ck_\perp(E_{\perp,2}/E_{\perp,1})}{\omega}. \tag{3.5}$$

We can determine the perturbed bulk velocity for each component $\mathbf{U}_s$ by recognizing that the total current linear density (including any parallel flow) due is $\mathbf{j}_s = q_s(n_{0s}\mathbf{U}_s + n_{1s}V_s\hat{\mathbf{z}})$. Using the susceptibility tensor to calculate $\mathbf{j}_s$ through (2.9) yields

$$\mathbf{U}_s = -\frac{i\omega}{4\pi q_s n_{0s}}\underline{\underline{\chi_s}}(\mathbf{k},\omega) \cdot \mathbf{E} - \frac{\delta n_s}{n_{0s}}V_s\hat{\mathbf{z}}. \tag{3.6}$$

With these solutions for the perturbed bulk velocity $\mathbf{U}_s$, we can use the linearized continuity equation (including the equilibrium parallel flow V_s),

$$\frac{\partial \delta n_s}{\partial t} + V_s\frac{\partial \delta n_s}{\partial z} = -n_{0s}\nabla \cdot \mathbf{U}_s, \tag{3.7}$$

to solve for the complex Fourier coefficient of the normalized number density fluctuation, $\delta n_s/n_{0s}$, given by

$$\frac{\delta n_{1s}}{n_{0s}} = \frac{k_\perp U_{xs} + k_{||}U_{zs}}{\omega - k_{||}V_s}. \tag{3.8}$$

We can also compute the power emitted or absorbed by each component, following the routines implemented in PLUME(Klein & Howes 2015), which follow Stix (1992)'s expression

$$\frac{\gamma_s(\mathbf{k})}{\omega_{\mathrm{r}}(\mathbf{k})} = \frac{\mathbf{E}^*(\mathbf{k}) \cdot \underline{\underline{\chi}}_s^a(\mathbf{k}) \cdot \mathbf{E}(\mathbf{k})}{4W_{\mathrm{EM}}(\mathbf{k})}, \tag{3.9}$$

where $\underline{\underline{\chi}}_s^a(\mathbf{k})$ represents the anti-Hermitian component of the susceptibility for species s evaluated at $\gamma = 0$ and $\mathbf{E}^*$ represents the complex conjugate of the fluctuating electric field, and W_{EM} is the electromagnetic wave energy.

TO DO: Currently working on implementing an additional diagnostic, already present in PLUME that splits the heating rates into transit time, Landau, and cyclotron damping components, following prescription laid out in Appendix C of Huang *et al.* (2024).

3.1. *Integration Near Poles*

We use a simple trapezoidal integration scheme. This scheme breaks down near poles, e.g. integrals of the form

$$I(p_\perp) = \int_{-\infty}^{\infty} dp_\parallel \frac{\Omega_j U \underline{\underline{T}}_n}{\omega - k_\parallel v_\parallel - n\Omega_j}. \tag{3.10}$$

When the imaginary component γ of the complex frequency $\omega = \omega_{\mathrm{r}} + i\gamma$ is sufficiently small, the denominator of the integral becomes small enough to lead to large numerical errors. We currently resolve this issue by rewriting the integral as

$$\mathcal{I} = \int_{-\infty}^{\infty} dx \frac{g(x)}{x - t_r - it_i} \tag{3.11}$$

evaluating it over a narrow symmetric interval,

$$\mathcal{I} = \int_{t_r - \Delta}^{t_r + \Delta} dx \frac{g(x)}{x - t_r - it_i} + \text{rest} \tag{3.12}$$

and then decomposing the integrand near t_r into odd (which disappears over the symetric integral) and even parts,

$$\mathcal{I} = \quad \frac{1}{2} \int_{t_r - \Delta}^{t_r + \Delta} dx \left[\frac{g(x)}{x - t_r - it_i} - \frac{g(2t_r - x)}{-x + t_r - it_i} \right] \tag{3.13}$$

$$+ \frac{1}{2} \int_{t_r - \Delta}^{t_r + \Delta} dx \left[\frac{g(x)}{x - t_r - it_i} + \frac{g(2t_r - x)}{-x + t_r - it_i} \right] + \text{rest}. \tag{3.14}$$

The even integral reduces to

$$\mathcal{I} = \int_{t_r}^{t_r + \Delta} dx \left[\frac{g(x)}{x - t_r - it_i} + \frac{g(2t_r - x)}{-x + t_r - it_i} \right] + \text{rest}. \tag{3.15}$$

We then perform a trapezoidal scheme over a fine grid between t_r and $t_r + \Delta$, which works as long at $|t_i|$ isn't too small. If $|t_i|$ is too small, we performing a truncated Taylor expansion to reduce these numerical errors

$$\mathcal{I} = \int_{t_r}^{t_r + \Delta} dx \left[\frac{2it_i g(t_r)}{(x - t_r)^2 + t_i^2} + \frac{2g'(t_r)(x - t_r)^2}{(x - t_r)^2 + t_i^2} \right] + \text{rest}. \tag{3.16}$$

where the first term on the right hand side can be expressed as it's small-t_i limit

$$\int_{t_r}^{t_r + \Delta} dx \frac{2it_i g(t_r)}{(x - t_r)^2 + t_i^2} = i\pi g(t_r)\text{sgn}(t_i). \tag{3.17}$$

These results converge, but are numerically expensive to evaluate, and currently require the user to specify when to switch between the two methods of evaluation, making future improvements to the numerical integration schemes that can more directly handle singularities a priority.

3.2. *Hybrid Analytic Continuation*

When the solutions are damped ($\gamma < 0$) the integration of Eqn. 2.17 necessitates an analytic continuation of $f_{0,s}$ into the complex $p_\parallel$ plane. This is 'simple' enough if $f_{0,s}$ is a known analytic function, evaluating the distribution at a complex $p_\parallel$† As we only

---

† Again, the relativistic case is more complex, given the non-trivial momentum dependence of the resonant denominator in that limit; see §3.3 fromVerscharen *et al.* (2018) gory details, where we use the method suggested by Lerche (1967) to transform from $(p_\parallel, p_\perp)$ to $(\Gamma, \bar{p}_\parallel)$ and make the solution tractable.

have a value for $f_{0,s}$ for $\mathbf{p} \in \mathcal{R}$, we adopt two different schemes to numerical extend the function.

For both cases, we follow Landau (1946)'s prescription for the integration of a contour C_L that lies below the complex poles of the integrand:

$$I(p_\perp) = \int_{C_L} \mathrm{d}p_\| G(p_\perp, p_\|) = \begin{cases} \int_{-\infty}^{+\infty} \mathrm{d}p_\| G(p_\perp, p_\|) & \text{if } \gamma > 0, \\ \mathcal{P} \int_{-\infty}^{+\infty} \mathrm{d}p_\| G(p_\perp, p_\|) + i\pi \sum \mathrm{Res}_A(G) & \text{if } \gamma = 0, \\ \int_{-\infty}^{+\infty} \mathrm{d}p_\| G(p_\perp, p_\|) + 2i\pi \sum \mathrm{Res}_A(G) & \text{if } \gamma < 0, \end{cases} \quad (3.18)$$

For our case, G has one simple pole

$$\sum \mathrm{Res}_A(G) = -\frac{m_j}{|k_\||}\Omega_j U\underline{\underline{T}}_n \bigg|_{p_\| = p_{\mathrm{pole}}}, \quad (3.19)$$

that has to be evaluated for the six unique terms in $\underline{\underline{T}}_n$. This can be done in two different ways, either through a fit of $f_{0,s}$ to an arbitrary number of analytic functions, or by a polynomial basis representation using a generalized linear least squares approach. One The code evaluates the fits separately at each $p_\perp$, so that no assumption is made as to the structure of f_{0s} in the $p_\perp$-direction. **ALPS uses these functions only if a pole is within the integration domain (the momentum range provided in the input VDF grid) and only if $\gamma \leqslant 0$.**

3.2.1. *Old Approach: Functional Fitting*

In the classic (2018) version of ALPS, in order to calculate the analytic continuation, we allowed the user to specify an arbitrary number (usually 1 or 2, corresponding to core-and-beam structures seems in in-situ solar wind observations) of analytic functions, each with their own handful of defining parameters. The cannonical case was used drifting bi-Maxwellians

$$f_{0j} = \frac{1}{\pi^{3/2} m_j^3 w_{\perp j}^2 w_{\|j}} \exp\left(-\frac{p_\perp^2}{m_j^2 w_{\perp j}^2} - \frac{(p_\| - m_j U_j)^2}{m_j^2 w_{\|j}^2} \right), \quad (3.20)$$

but bi-kappa

$$f_{0j} = \frac{1}{m_j^3 w_{\perp j}^2 w_{\|j}} \left[\frac{2}{\pi(2\kappa - 3)} \right]^{3/2} \frac{\tilde{\Gamma}(\kappa+1)}{\tilde{\Gamma}(\kappa-1/2)} \quad (3.21)$$

$$\times \left\{ 1 + \frac{2}{2\kappa - 3} \left[\frac{p_\perp^2}{m_j^2 w_{\perp j}^2} + \frac{(p_\| - m_j U_j)^2}{m_j^2 w_{\|j}^2} \right] \right\}^{-(\kappa+1)}, \quad (3.22)$$

($\tilde{\Gamma}$ is the Gamma function, not to be confused with the Lorentz factor Γ) and Jüttner distributions

$$f_{0j} = \frac{1}{2\pi m_j^3 c w_j^2 K_2(2c^2/w_j^2)} \exp\left(-2\frac{c^2}{w_j^2}\sqrt{1 + \frac{|p|^2}{m_j^2 c^2}} \right); \quad (3.23)$$

were also included in the initial release. Additional functions, including two other representations of the Jüttner distribution as well as a bi-Moyal distribution

$$f_{0,j}(\hat{p}_\perp, \hat{p}_\|) = u_1 \exp[0.5(yu_4\hat{p}^2\_\perp + u_2(\hat{p}\_\| - u_3)^2 - \exp(yu_4\hat{p}^2\_\perp + u_2(\hat{p}\_\| - u_3)^2))], \quad (3.24)$$

were added based upon community request. At each $p_\perp$ value, a 1-D automated Levenberg-Marquardt fit is performed as a function of $p_\|$ (Levenberg 1944; Marquardt 1963). For $p_\perp = 0$, the user defined initial guesses are used to start the fit; the code then

iterates to larger $p_\perp$ values, using the best fit values from the previous $p_\perp$ array as initial guesses for the $p_\perp$ array. This process works well for sufficiently smooth functions, and close enough initial guesses. However, in applying the code to more complicated VDFs, two obvious difficulties arose;

1) Even when a good set of initial guesses were selected, the fitting routine could fail at larger $p_\perp$ values, causing the entire code to halt.

2) Even when the fits converged, the small number of functions used for the analytic representation lead to discrepancies as solutions pass $\gamma = 0$. These discrepancies arise for two reasons:

- The velocity derivative of $f_{0j}[(\omega - n\Omega_s)/k_\parallel]$ is discontinuous when evaluated at $\gamma > 0$ and $\gamma < 0$.
- If the velocity moments of the fit (e.g. the density or the bulk velocity) are different from the velocity moments of the actual VDF, the total charge and current will be different for the two halves of the complex plane.

These discrepancies can be small, leading to slight differences that don't impact the mode structure, but can lead to a 'sharp edge' that causes the numerical (e.g. Newton-secant) search to jump solutions (or lose the solution entirely).

These discrepancies can also be large, especially if the net current is significantly different between the input VDF and the fitted function(s).

These issues lead to the development of a new approach to perform the hybrid analytic continuation, a polynomial basis representation.

3.2.2. *New Approach: Polynomial Basis Representation*

Instead of representing $f_{0,s}$ with one or a handful of physically representative fitted analytic functions, we have (over the last few months) opted to instead implement a General Linear Least Squares fit (§15.4 of Press *et al.* 1992) of $f_0(p_\perp, p_\parallel)$. Specifically, we are finding the parameters a_k for the model

$$y(x) = \sum_{k=0}^{M-1} a_k X_k(x) \tag{3.25}$$

where $X_k(x)$ are our basis functions. For the initial implementation, we have selected the Chebyshev polynomials of the first kind $T_k(x)$ as the basis function,

$$T_0(x) \qquad\quad = 1 \tag{3.26}$$
$$T_1(x) \qquad\quad = x \tag{3.27}$$
$$T_{n+1}(x\,) = 2xT_n(x) - T_{n-1}(x) \tag{3.28}$$

but we intend on allowing the user to select other basis functions as an future code option, e.g. the ever popular Hermite functions (Zocco & Schekochihin 2011; Adkins & Schekochihin 2018). As T_n are bound between $[-1, 1]$, we perform a change of variables from $p_\parallel$ to x

$$x = \frac{p_\parallel - \left(p_\parallel^{\mathrm{max}} + p_\parallel^{\mathrm{min}}\right)/2}{\left(p_\parallel^{\mathrm{max}} - p_\parallel^{\mathrm{min}}\right)/2} \tag{3.29}$$

where $p_\parallel^{\mathrm{max,min}}$ are the maximum and minimum values of the input VDF grid. Additionally, we fit to $\log_{10}[f_{s0}]$ rather than f_{s0} to cover the full range of VDF structure and not soley the structure near the peak.

As with the functional fitting approach, this is a purely one dimensional method, fitting

$f_{0,s}(p_\parallel)$ separately for the $n_\perp$ rows in the input VDF grid; we write the VDF slice that we will be fitting as y_i, which is known at N values of x.

The solution is performed via the 'Normal Equations', solving

$$\sum_{j=0}^{M-1} \alpha_{kj} a_j = \beta_k \tag{3.30}$$

where

$$\alpha_{kj} = \sum_{i=0}^{N-1} \frac{X_j(x_i) X_k(x_i)}{\sigma_i^2} \tag{3.31}$$

and

$$\beta_k = \sum_{i=0}^{N-1} \frac{y_i X_k(x_i)}{\sigma_i^2}. \tag{3.32}$$

If errors in the knowledge of y_i are known, one could set σ_i to non-unity values; for now, we have set to $1 \forall x_i$. Eqn. 3.30 is solved using the `dgemm`, `dgemv`, and `dgesv` LAPACK routines.

In comparisons between the two hybrid analytic continuation methods, the polynomial basis produces the same results for simple VDFs as the functional fitting method, and is superior to previous functional fitting method for very 'wiggly' VDFs in terms of its smoothness across γ, due to improved accuracy of $\partial_v f_{0,j}$ for all ω and $\mathbf{k}$ values, as well as and in correctly capturing the component density and current.

To illustrate this, let's choose a **pathological** case†. Fig. 1 illustrates the fitting of a slice of $f_p(p_\parallel)$ for $p_\perp = 0$ using the old core+beam method, as well as the updated GLLS method. We can see that the representation of f_p does not match the actual at all points in $p_\parallel$. Additionally, the value of the proton current $\int dv v_\parallel f_p(v)$ is -0.153 $q_p n_p v_A$, compared to $0.0023561 q_p n_p v_A$ for the direct integration of the input f_p. As the electrons are set to have a current balancing the integrated current, the core+beam representation has a discontinuity in the represented current as the solution passes over $\gamma = 0$, leading to abrupt changes in the mode structure for $\gamma < 0$.

To suggest the necessary order for the GLLS method, consider Fig. 2

So, are the modes that `ALPS` finds real? To investigate this, we consider the actual proton VDF, for this case taken from a Wind spacecraft observations, f_{wind}, as well as a two-component proton VDF of the best fit to the actual proton VDF, f_{bM}. At each point in $v_\perp, v_\parallel$, we calculate $\Delta f \equiv f_{wind} - f_{bM}$, and then construct N VDFs that smoothly vary between the two extreme cases,

$$f_i(v_\perp, v_\parallel) = f_{wind}(v_\perp, v_\parallel) + \frac{i \Delta f(v_\perp, v_\parallel)}{N-1} \tag{3.33}$$

for $i \in [0, N]$.

The normal mode structure for these solutions at a fixed $(k_\perp, k_\parallel) d_p = (0.001, 0.0025)$ is illustrated in Fig. 3. We see that at this wavevector, some of the modes are unaffected, e.g. the forward Alfvén and fast modes, while the compressive modes and especially the backwards fast mode has a significant change in the damping rate. The fact that we have a continuous path for the solutions of f_i is indicative that the solutions are are least mathematically correct.

† Note that the cases investigated in Walters *et al.* (2023) did not have this magnitude of an unphysical current added via the the hybrid analytic continuation with the core+beam fitting; repeating those calculations with the GLLS method yields quantitatively similar results.
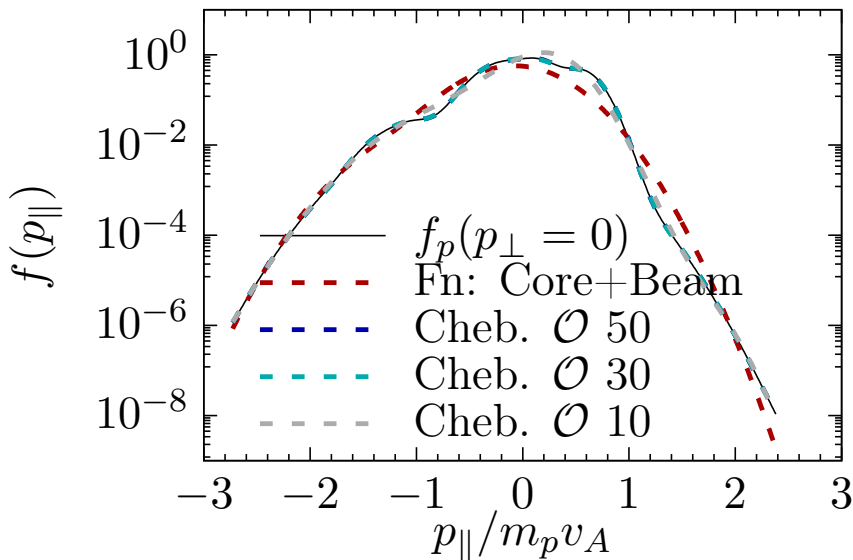
FIGURE 1. Comparison of $f_{p,0}(p_\perp = 0, p_\parallel)$ (black line) representations using a two Maxwellian (red) method compared to three GLLS fits with Chebyshev functions.

So, does the stability of these solutions change? In Fig. 4, we plot the $[\omega_r, gamma](k_\parallel)$ dispersion relations for eight solutions, namely the slow, Alfven, fast forward and backward waves and the two $\omega \sim 0$ 'entropy' modes for fixed $k_\perp d_p = 0.001$.‡ We see that, for most of the solutions, ω_r remains relatively unchanged, with two exceptions; the forward fast and slow modes appear to undergo a mode conversion, similar to those seen near exceptional points ¶ and the strong damping of the proton cyclotron resonance acts to slow, and eventually reverse, the propagation direction of the Alfven solution at different $k_\parallel$ values for different f_i's. The regions of wavevector support for unstable mode growth, as well as the amplitude of the most unstable mode, do change for the Alfven solutions. To better highlight this behavior, we plot in Fig. 5 a parameteric plot of the dispersion relations. The changes in which modes are unstable (e.g. the Forward Alfven solution is effectively stable in the bi-Maxwellian representation, while it becomes unstable for the f_{wind} case), as well as the frequencies that resonant with f_p to drive the backwards Alfvén ion-cyclotron instability.

Open Question: how far to extend into complex momentum space?

How large of a $\mathcal{I}m(p_\parallel)$ should we trust these extensions?

‡ See discussion in §2 of Verscharen *et al.* (2016) and Kunz *et al.* (2020) for detailed discussions of slow and entropy modes.

¶ Exceptional points satisfy $|\Lambda(\omega)| = 0$ and $d_\omega|\Lambda(\omega)| = 0$ and act as branch points that allow continuous variations in f to smoothly vary between different normal mode solutions; c.f. the Appendix of Klein & Howes (2015)
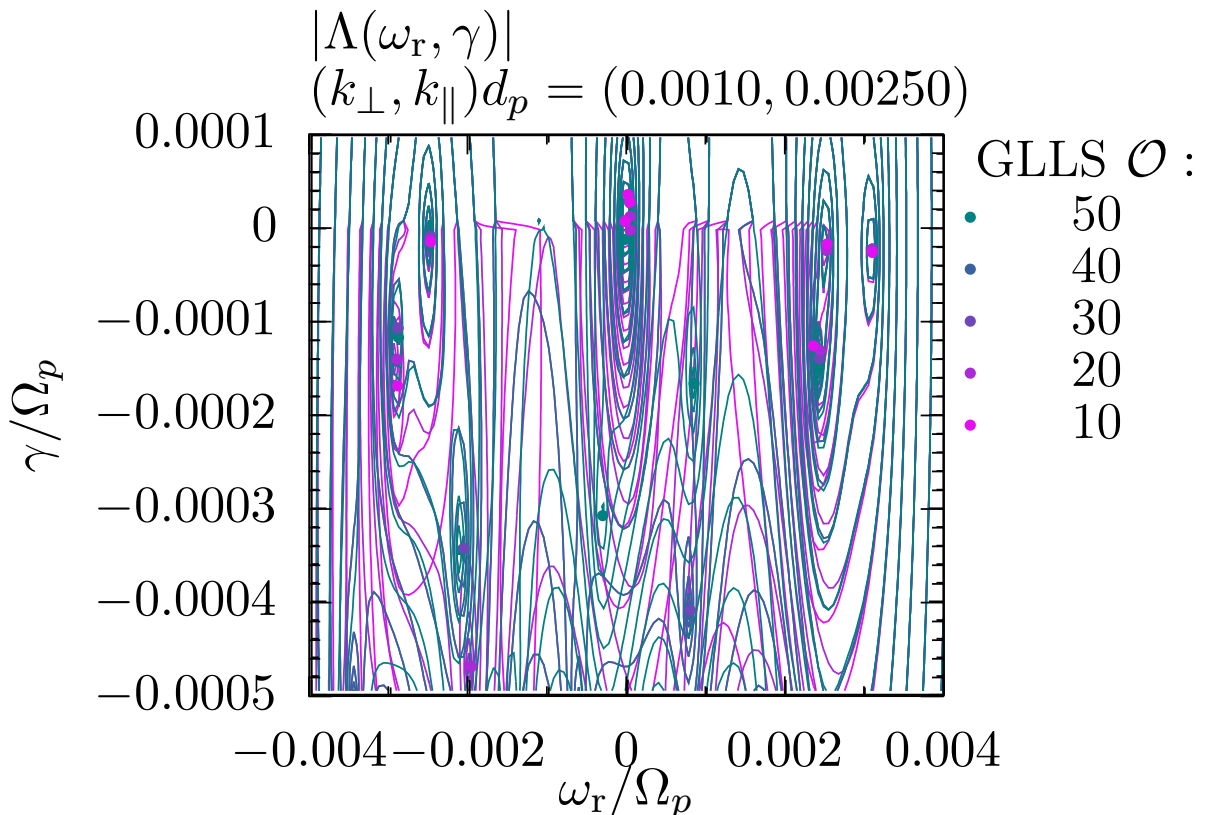
FIGURE 2. Isocontours of constant Λ for ALPSsolutions GLLS analytic continuation with varying orders of Chebyshev polynomials. Identified solutions with $\Lambda = 0$ are shown with dots. Poor solutions for the $\mathcal{O}(10)$ fit illustrate the discontinuity across $\gamma = 0$, while nearly identical normal mode solutions for $\mathcal{O}(40)$ and $\mathcal{O}(50)$ suggest a convergence for the description of the damped mode solutions.

3.3. *Specifying Analytic Functions*

Since the 2018 code release, we have also added to ALPS the ability to specify any analytic form for $f(v_\perp, v_\parallel)$, which allows the direct calculation of the appropriate integrals on a specified grid, as well as the immediate extension to complex $p_\parallel$ values with out the need for any fitting or polynomial representations. While useful, this isn't directly applicable to cases where a simulation or model isn't easily expressible in analytic form, but can be quite useful when a theory predicts an analytic form (e.g. a bi-Moyal flattop distribution) so that differences against standard bi-Maxwellian predictions can be quantified.

3.4. *'Hybrid' Treatment for Select Components*

For numerical expediency, the code allows users to declare if a component is to be treated as a known analytic function, e.g. if the electrons can be treated as a biMaxwellian, specifically using the formalism from NHDS (Verscharen & Chandran 2018). In these cases, the susceptibility for those components are calculated using the much more numerically efficient bi-Maxwellian expressions, rather than direct integration of the
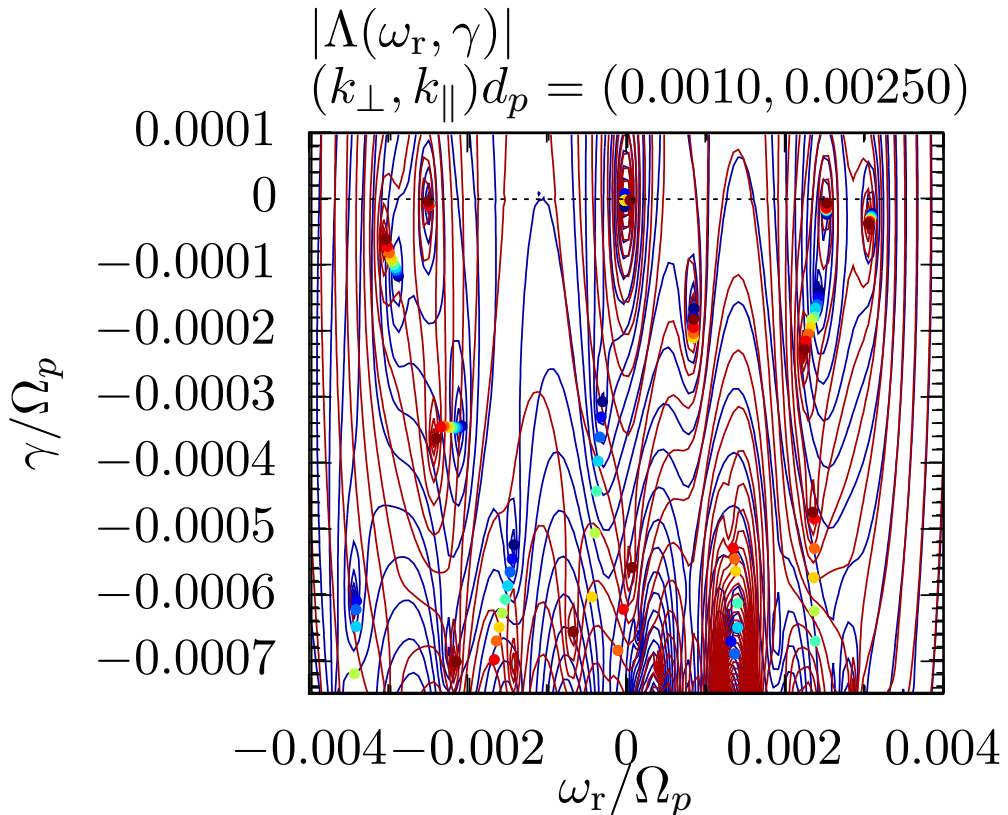
FIGURE 3. Isocontours of constant Λ for `ALPS`solutions using f_{wind} (blue lines) and f_{bM} (red). Identified solutions with $\Lambda = 0$ are shown with dots, with the f_i cases illustrated connecting the blue and red solutions.

momentum derivatives. This 'hybrid approach' significantly decreases the computational costs, and is quite useful in cases where some of the components are fairly treated as cold or a simple Maxwellian, e.g. evaluating hybrid nonlinear plasma simulations.

4. Open Questions and Future Calculations

4.1. *Improved Numerical Methods*

As noted in several of the subsections, many of the numerical methods are fairly basic implementations, e.g. trapezoidal integration, and should be improved; any suggestions on better methods that have worked for other kinetic systems would be appreciated. This will be quite helpful for

4.2. *'Automated' Instability Determination*

Determining if a plasma is unstable can be a time consuming hunt across complex frequency space. Rather than inspecting the pole structure over the (ω_r, γ), one can
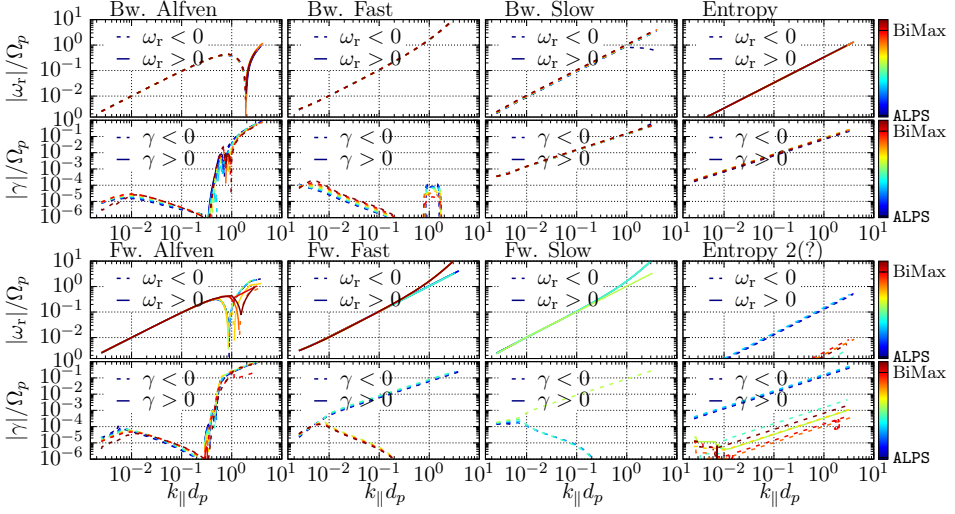
FIGURE 4. Dispersion relations for eight normal mode solutions for $k_\perp d_p = 0.001$ and varying $k_\parallel d_p$ calculated using ALPSfrom the extreme f_{wind} and f_{bM} arrays, as well as the intermediate f_i cases.
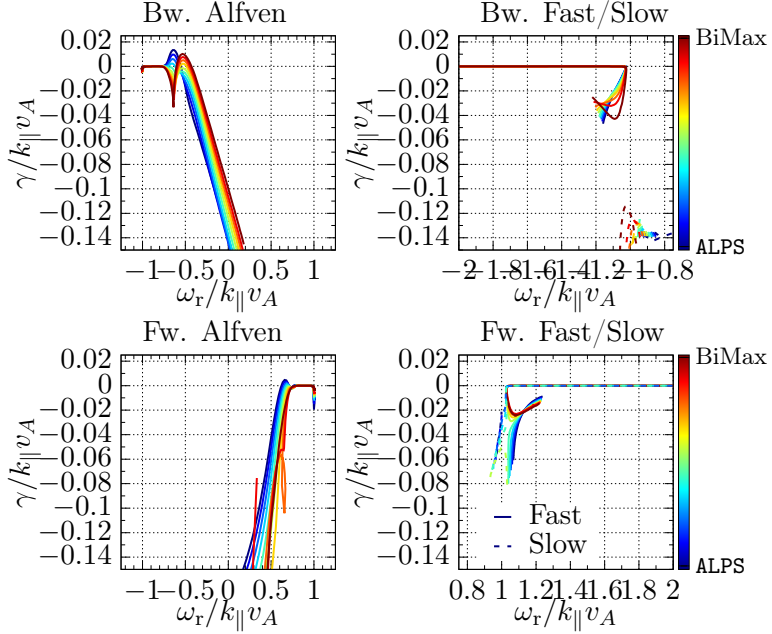
FIGURE 5. Parameteric plots of $\omega_r, \gamma](k_\parallel, d_p)$ dispersion relations for the Alfven, fast, and slow solutions.

follow Nyquist (1932) and simply integrate the contour integral

$$W_n(\mathbf{k}) = \frac{1}{2\pi i} \oint \frac{d\omega}{\det |\Lambda(\omega, \mathbf{k})|} \tag{4.1}$$
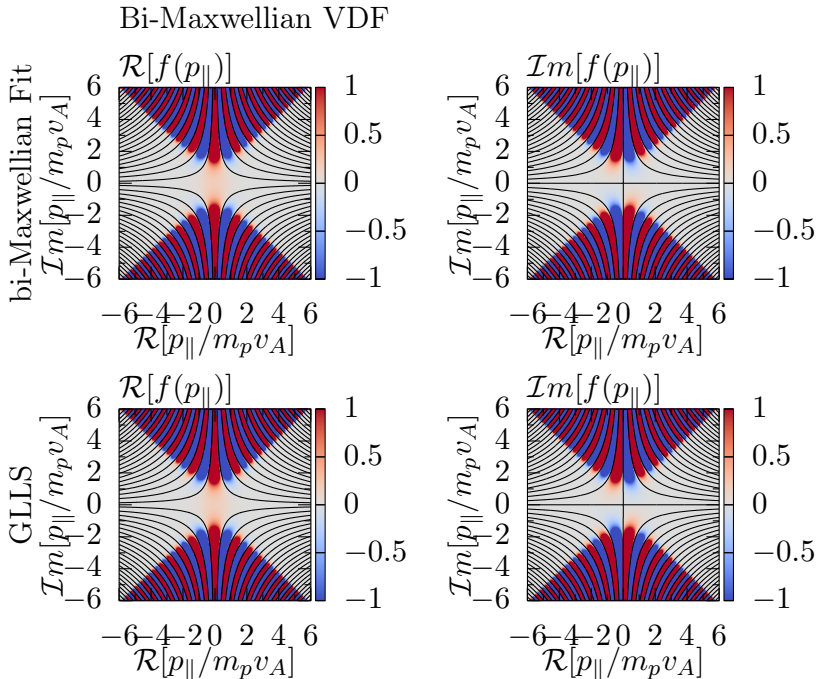
Bi-Maxwellian VDF

FIGURE 6. The real (left column) and imaginary (right column) components of the continued distribution into the complex parallel momentum plane, evaluated using either a bi-Maxwellian fit (top row) or the GLLS routine for 50 order fit.

As $\det |\Lambda(\omega, \mathbf{k})| = 0$ represents the normal modes solutions of the plasma, when taking the contour in Eqn. 4.1 over the upper half plane we get a count of the number of unstable modes with $\gamma > 0$ (see Fig. 8) By iteratively performing the contour integral along path parallel to but above the real axis, we can additionally determine the growth rate of the fastest growing mode.

It can be shown that an equivalent method of evaluating Eqn 4.1 is to map the value of $|\Lambda|^{-1}$ along the line from $(\omega_{\rm r} \to -\infty, \gamma = 0)$ to $(\omega_{\rm r} \to \infty, \gamma = 0)$ to a parametric curve in $(|\Lambda|_R^{-1}, |\Lambda|_I^{-1})$ space where R and I identify the real and imaginary components of the complex valued $|\Lambda|^{-1}$. constructing a "Nyquist diagram." The number of times this curve encircles the origin $(|\Lambda|_R^{-1}, |\Lambda|_I^{-1}) = (0, 0)$, an integer defined as the winding number W_n, equals the number of unstable normal modes the system supports. We evaluate this number using established methods from applied maths Shimrat (1962); Hormann & Agathos (2001), illustrated in Fig. 9.

This has been implemented for the bi-Maxwellian solver PLUME, (Klein *et al.* 2017, 2019; Martinović *et al.* 2021), but as of yet hasn't been applied to ALPS due to the computational cost of calculating $\Lambda(\omega, \mathbf{k})$.

4.3. *Non-Gyrotropy*

Especially near shocks and other discontinuities, the VDFs can become significantly agyrotropic, with these departures driving a plethora of instabilities, e.g. the electron cyclotron drift instability (ECDI) (Forslund *et al.* 1970; Umeda *et al.* 2012). Re-working the maths between Eqn. 2.16 and 2.17 without integrating over the gyrophase of the particles is a possible direction for an extension of, or a successor code to, ALPS.
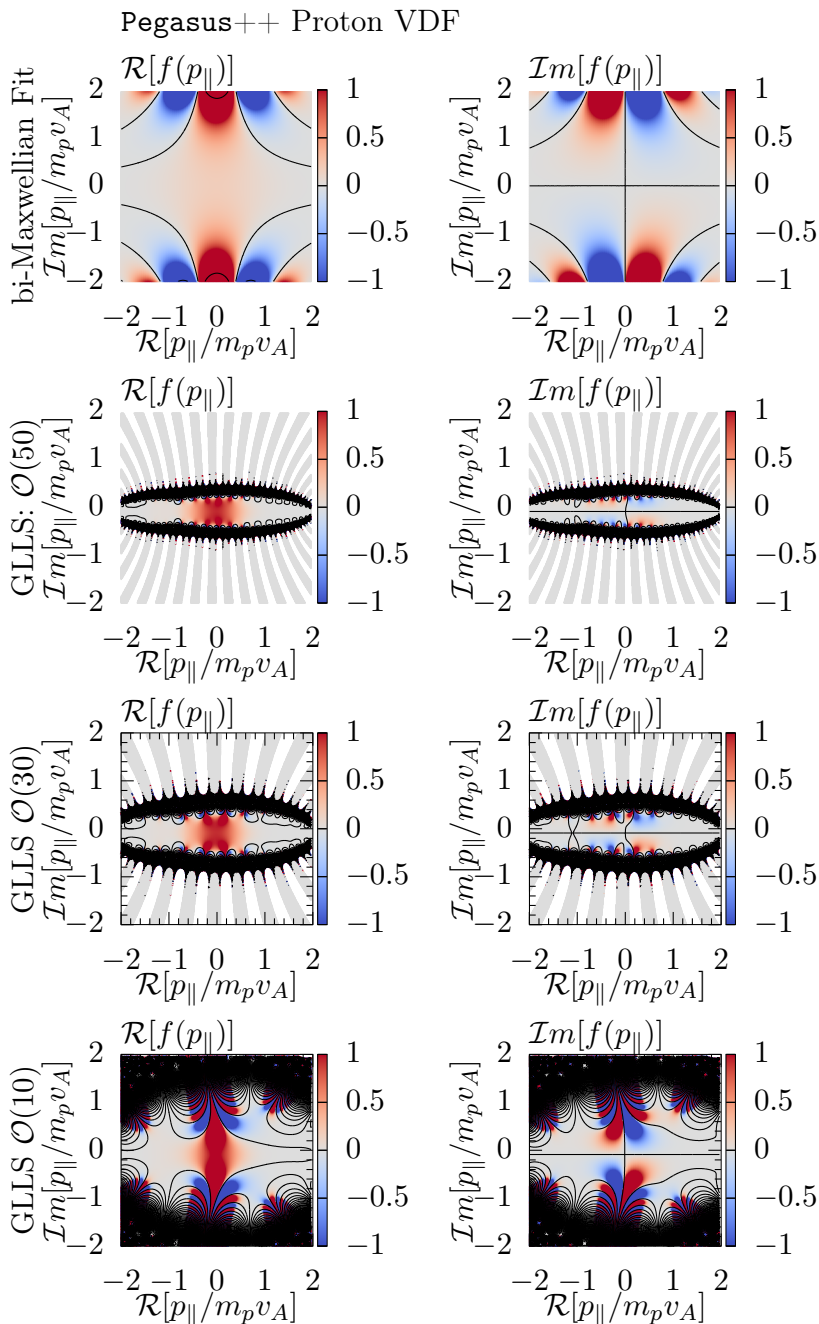
FIGURE 7. Columns as Fig. 6, but for a more realistic VDF (drawn from a Pegasus++ nonlinear simulation of imbalanced turbulence), comparing the continuation of f_p for the bi-Maxwellian fit, as well as GLLS fits of order 50, 30, and 10.
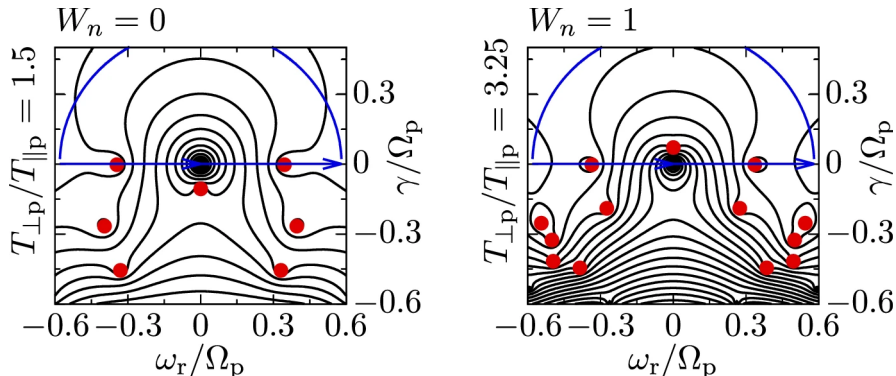
FIGURE 8. Instability calculation via the Nyquist criterion contour integral evaluation. The number of solutions (red dots) inside the blue contour represent the number of unstable modes; at left is a stable case, while at right, the additional temperature anisotropy has made the zero-frequency mode mirror unstable. Repeatedly shifting the blue line to larger γ values will result in an identification of the maximum growth rate, the number of solutions in the contour will drop to zero. Reproduced from Verscharen *et al.* (2019).
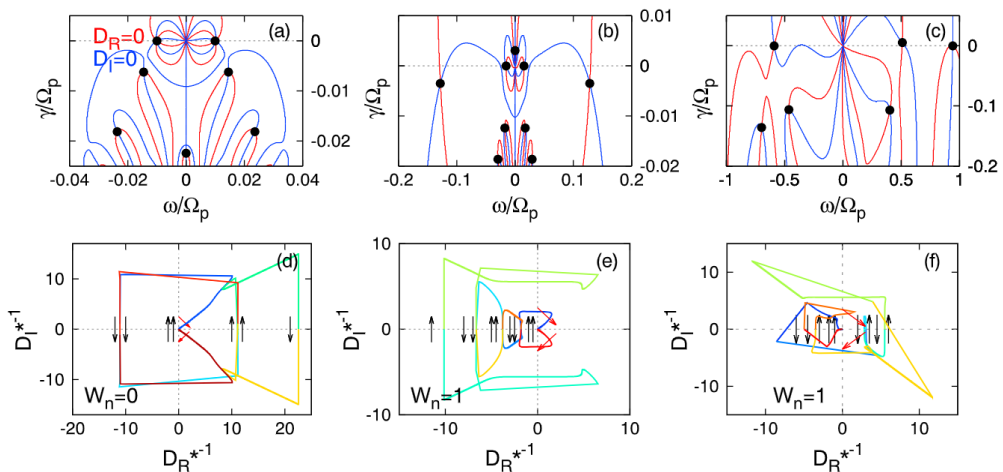
FIGURE 9. Schematic of winding number counting method for stable (left) and two unstable cases. Taken from Klein *et al.* (2017)

4.4. *Spatial Inhomogeneity*

Rumor has it that this was discussed in detail last week. I would be quite interested in discussing if/how `ALPS` could be extended to consider inhomogeneous systems.

4.5. *Self-Gravity*

If we replace the Lorentz force term in Eqn 2.15 with the appropriate self-gravity expressions, a stellar version of `ALPS` should be feasible to construct.

5. Code Availability

The code, written in `FORTRAN90`, is available via an open source BSD 2-Clause License at `https://github.com/danielver02/ALPS` with a full tutorial on its use at `https://danielver02.github.io/ALPS/` (Klein *et al.* 2023).

REFERENCES

ADKINS, T. & SCHEKOCHIHIN, A. A. 2018 A solvable model of Vlasov-kinetic plasma turbulence in Fourier-Hermite phase space. *Journal of Plasma Physics* **84** (1), 905840107, arXiv: 1709.03203.

ASTFALK, PATRICK, GÖRLER, TOBIAS & JENKO, FRANK 2015 DSHARK: A dispersion relation solver for obliquely propagating waves in bi-kappa-distributed plasmas. *Journal of Geophysical Research (Space Physics)* **120** (9), 7107–7120.

FORSLUND, D. W., MORSE, R. L. & NIELSON, C. W. 1970 Electron Cyclotron Drift Instability. *Phys. Rev. Lett.* **25** (18), 1266–1270.

GARY, S. P. 1993 *Theory of Space Plasma Microinstabilities*.

HORMANN, KAI & AGATHOS, ALEXANDER 2001 The point in polygon problem for arbitrary polygons. *Computational Geometry* **20** (3), 131–144.

HUANG, RUI, HOWES, GREGORY G. & MCCUBBIN, ANDREW J. 2024 The Velocity-Space Signature of Transit-Time Damping. *arXiv e-prints* p. arXiv:2401.16697, arXiv: 2401.16697.

JIANG, WENCE, VERSCHAREN, DANIEL, JEONG, SEONG-YEOP, LI, HUI, KLEIN, KRISTOPHER G., OWEN, CHRISTOPHER J. & WANG, CHI 2024 Velocity-space Signatures of Resonant Energy Transfer between Whistler Waves and Electrons in the Earth's Magnetosheath. *Astrophys. J.* **960** (1), 30, arXiv: 2311.17309.

JIANG, WENCE, VERSCHAREN, DANIEL, LI, HUI, WANG, CHI & KLEIN, KRISTOPHER G. 2022 Whistler Waves as a Signature of Converging Magnetic Holes in Space Plasmas. *Astrophys. J.* **935** (2), 169, arXiv: 2207.00273.

KLEIN, K. G. & HOWES, G. G. 2015 Predicted impacts of proton temperature anisotropy on solar wind turbulence. *Phys. Plasmas* **22** (3), 032903, arXiv: 1503.00695.

KLEIN, KRISTOPHER G., KASPER, JUSTIN C., KORRECK, K. E. & STEVENS, MICHAEL L. 2017 Applying nyquist's method for stability determination to solar wind observations. *J. Geophys. Res.* p. 981509823, 2017JA024486.

KLEIN, KRISTOPHER G., KASPER, JUSTIN C., KORRECK, K. E. & STEVENS, MICHAEL L. 2017 Applying Nyquist's method for stability determination to solar wind observations. *Journal of Geophysical Research (Space Physics)* **122**, 9815–9823.

KLEIN, KRISTOPHER G., MARTINOVIĆ, MIHAILO, STANSBY, DAVID & HORBURY, TIMOTHY S. 2019 Linear Stability in the Inner Heliosphere: Helios Re-evaluated. *Astrophys. J.* **887** (2), 234, arXiv: 1912.00250.

KLEIN, K. G., VERNIERO, J. L., ALTERMAN, B., BALE, S., CASE, A., KASPER, J. C., KORRECK, K., LARSON, D., LICHKO, E., LIVI, R., MCMANUS, M., MARTINOVIĆ, M., RAHMATI, A., STEVENS, M. & WHITTLESEY, P. 2021 Inferred Linear Stability of Parker Solar Probe Observations Using One- and Two-component Proton Distributions. *Astrophys. J.* **909** (1), 7, arXiv: 2101.10937.

KLEIN, K. G., VERSCHAREN, D., KOSKELA, T & STANSBY, D 2023 danielver02/alps: Zenodo release.

KUNZ, M. W., SQUIRE, J., SCHEKOCHIHIN, A. A. & QUATAERT, E. 2020 Self-sustaining sound in collisionless, high-β plasma. *Journal of Plasma Physics* **86** (6), 905860603, arXiv: 2006.08940.

LANDAU, L. D. 1946 On the vibrations of the electronic plasma. *J. Phys.(USSR)* **10**, 25–34, [Zh. Eksp. Teor. Fiz.16,574(1946)].

LERCHE, I. 1967 Unstable Magnetosonic Waves in a Relativistic Plasma. *Astrophys. J.* **147**, 689.

LEVENBERG, KENNETH 1944 A method for the solution of certain non-linear problems in least squares. *Quarterly of Applied Mathematics* **2** (2), 164–168.

MARQUARDT, DONALD W. 1963 An algorithm for least-squares estimation of nonlinear

parameters. *Journal of the Society for Industrial and Applied Mathematics* **11** (2), 431–441.

MARTINOVIĆ, MIHAILO M., KLEIN, KRISTOPHER G., ĎUROVCOVÁ, TEREZA & ALTERMAN, BENJAMIN L. 2021 Ion-driven Instabilities in the Inner Heliosphere. I. Statistical Trends. *Astrophys. J.* **923** (1), 116, arXiv: 2110.07772.

MCMANUS, MICHAEL D., KLEIN, KRISTOPHER G., BALE, STUART D., BOWEN, TREVOR A., HUANG, JIA, LARSON, DAVIN, LIVI, ROBERTO, RAHMATI, ALI, ROMEO, ORLANDO, VERNIERO, JAYE & WHITTLESEY, PHYLLIS 2024 Proton- and Alpha-driven Instabilities in an Ion Cyclotron Wave Event. *Astrophys. J.* **961** (1), 142, arXiv: 2310.14136.

NYQUIST, HARRY 1932 Regeneration theory. *Bell system technical journal* **11** (1), 126–147.

PRESS, W. H., TEUKOLSKY, S. A., VETTERLING, W. T. & FLANNERY, B. P. 1992 *Numerical recipes in FORTRAN. The art of scientific computing*.

ROENNMARK, K. 1982 Waves in homogeneous, anisotropic multicomponent plasmas (WHAMP). *Tech. Rep.*.

SHIMRAT, M. 1962 Algorithm 112: Position of point relative to polygon. *Commun. ACM* **5** (8), 434.

STIX, T. H. 1992 *Waves in plasmas*. American Institute of Physics.

UMEDA, TAKAYUKI, KIDANI, YOSHITAKA, MATSUKIYO, SHUICHI & YAMAZAKI, RYO 2012 Microinstabilities at perpendicular collisionless shocks: A comparison of full particle simulations with different ion to electron mass ratio. *Physics of Plasmas* **19** (4), 042109–042109, arXiv: 1204.2539.

VERSCHAREN, D., BOUROUAINE, S., CHANDRAN, B. D. G. & MARUCA, B. A. 2013 A Parallel-propagating Alfvénic Ion-beam Instability in the High-beta Solar Wind. *Astrophys. J.* **773**, 8, arXiv: 1306.2531.

VERSCHAREN, DANIEL & CHANDRAN, BENJAMIN D. G. 2018 NHDS: The New Hampshire Dispersion Relation Solver. *Research Notes of the American Astronomical Society* **2** (2), 13, arXiv: 1804.10096.

VERSCHAREN, D., CHANDRAN, B. D. G., KLEIN, K. G. & QUATAERT, E. 2016 Collisionless Isotropization of the Solar-wind Protons by Compressive Fluctuations and Plasma Instabilities. *Astrophys. J.* **831**, 128, arXiv: 1605.07143.

VERSCHAREN, D., KLEIN, K. G., CHANDRAN, B. D. G., STEVENS, M. L., SALEM, C. S. & BALE, S. D. 2018 ALPS: the Arbitrary Linear Plasma Solver. *Journal of Plasma Physics* **84** (4), 905840403, arXiv: 1803.04697.

VERSCHAREN, DANIEL, KLEIN, KRISTOPHER G. & MARUCA, BENNETT A. 2019 The multi-scale nature of the solar wind. *Living Rev. Solar Phys.* **16** (1), 5, arXiv: 1902.03448.

WALTERS, JADA, KLEIN, KRISTOPHER G., LICHKO, EMILY, STEVENS, MICHAEL L., VERSCHAREN, DANIEL & CHANDRAN, BENJAMIN D. G. 2023 The Effects of Nonequilibrium Velocity Distributions on Alfvén Ion-cyclotron Waves in the Solar Wind. *Astrophys. J.* **955** (2), 97, arXiv: 2308.14944.

ZOCCO, ALESSANDRO & SCHEKOCHIHIN, ALEXANDER A. 2011 Reduced fluid-kinetic equations for low-frequency dynamics, magnetic reconnection, and electron heating in low-beta plasmas. *Physics of Plasmas* **18** (10), 102309–102309, arXiv: 1104.4622.